nature catalysis

ARTICLES

https://doi.org/10.1038/s41929-019-0383-7

Cooperative CO_2-to-ethanol conversion via enriched intermediates at molecule–metal catalyst interfaces

Fengwang Li[1,3], Yuguang C. Li[1,3], Ziyun Wang[1,3], Jun Li[1,2,3], Dae-Hyun Nam[1], Yanwei Lum[1], Mingchuan Luo[1], Xue Wang[1], Adnan Ozden[2], Sung-Fu Hung[1], Bin Chen[1], Yuhang Wang[1], Joshua Wicks[1], Yi Xu[2], Yilin Li[1], Christine M. Gabardo[2], Cao-Thang Dinh[1], Ying Wang[1], Tao-Tao Zhuang[1], David Sinton[2] and Edward H. Sargent[1]*

Electrochemical conversion of CO_2 into liquid fuels, powered by renewable electricity, offers one means to address the need for the storage of intermittent renewable energy. Here we present a cooperative catalyst design of molecule–metal catalyst interfaces with the goal of producing a reaction-intermediate-rich local environment, which improves the electrosynthesis of ethanol from CO_2 and H_2O. We implement the strategy by functionalizing the copper surface with a family of porphyrin-based metallic complexes that catalyse CO_2 to CO. Using density functional theory calculations, and in situ Raman and operando X-ray absorption spectroscopies, we find that the high concentration of local CO facilitates carbon–carbon coupling and steers the reaction pathway towards ethanol. We report a CO_2-to-ethanol Faradaic efficiency of 41% and a partial current density of 124 mA cm^{-2} at −0.82 V versus the reversible hydrogen electrode. We integrate the catalyst into a membrane electrode assembly-based system and achieve an overall energy efficiency of 13%.

The renewable-electricity-powered CO_2 reduction reaction (CO_2RR) offers a means to store intermittent electricity as dispatchable fuels and valuable chemical feedstocks[1,2]. Among the various products (CO, formic acid, methane, ethylene, ethanol and 1-proponal) formed from CO_2RR, ethanol (a liquid fuel or fuel additive) is desired because it is energy dense by volume and because it levers extensive existing infrastructure for the storage and distribution of carbon-based fuels[3,4]. However, electrochemical CO_2-to-ethanol conversion relies on multiple proton and electron transfers that involve multiple intermediates[5–7], making the development of more efficient electrocatalysts an important but also challenging problem.

Cu-based heterogeneous materials are distinctive among metal catalysts in their ability to reduce CO_2 to products with two or more carbon atoms (C_{2+}). Ethylene has, in past reports, been favoured two to fourfold over ethanol[8–11]. To steer the selectivity towards ethanol, the focus has been on the tuning of binding strength of reaction intermediates on Cu via doping using elements such as silver[12,13], and through the creation of grain boundaries[14] and vacancies[15]. These advances have increased the Faradaic efficiency (FE) towards ethanol to an impressive 30%. Technoeconomic assessment[4,16] suggests that further progress on FE, as well as on lowering the overpotential (today above 1 V at current densities above 10 mA cm^{-2}), are urgently needed; indeed, it is desired to increase half-cell cathodic energy efficiencies (CEEs) from today's level of ≤15% (refs. [11–13,15,17–20]) to >20% and beyond.

Scaling relations account for the fact that binding strengths of different intermediates on the same site (that is Cu) are correlated, which means that optimizing for one adsorbed species will typically take the other steps away from their optima[21,22]. We sought therefore to add a further degree of freedom in catalyst design that would influence predominantly one step. Specifically, we strove to increase the reaction rate of one step without strongly modulating the others, by judiciously increasing the coverage of one key intermediate, yet not interfering with the electronic structure (hence binding strength) of Cu, with the goal of circumventing the scaling relations.

Cu-based bimetallic catalysts have been reported to generate, on the doping metal sites, high-concentration CO, a key intermediate along C_{2+} pathways[23–25], to spill over to the Cu sites for improved carbon–carbon (C–C) coupling and further reduction to C_{2+} products[20,26,27]. However, the ratio of the heteroatom (Au, Ag, Zn) to Cu on the catalyst surface is low (for example, <2% in the case of Au and Cu (ref. [27])), resulting in a limited proportion of interfaces that offer local enrichment of intermediates. Further increasing this ratio modulates the electronic structure of Cu and then reduces selectivity towards C_{2+} products[27–29].

Here we present instead a molecule–metal composite material in which the molecular adsorbate generates a high concentration of the key early intermediate, CO, yet does not modulate the metallic active sites germane to the crucial C–C coupling step. Density functional theory (DFT) calculations indicate that the increased coverage of CO on Cu, achieved by increasing its concentration near the Cu surface, not only decreases the reaction energy for the C–C coupling step, but also steers the selectivity from ethylene to ethanol. We implement this concept experimentally by functionalizing a family of porphyrin-based metallic complexes capable of catalysing CO_2RR to CO on the Cu surface. The near-unity coverage of the complexes maximizes the local concentration of CO for the

[1]Department of Electrical and Computer Engineering, University of Toronto, Toronto, Ontario, Canada. [2]Department of Mechanical and Industrial Engineering, University of Toronto, Toronto, Ontario, Canada. [3]These authors contributed equally: Fengwang Li, Yuguang C. Li, Ziyun Wang.
*e-mail: ted.sargent@utoronto.ca

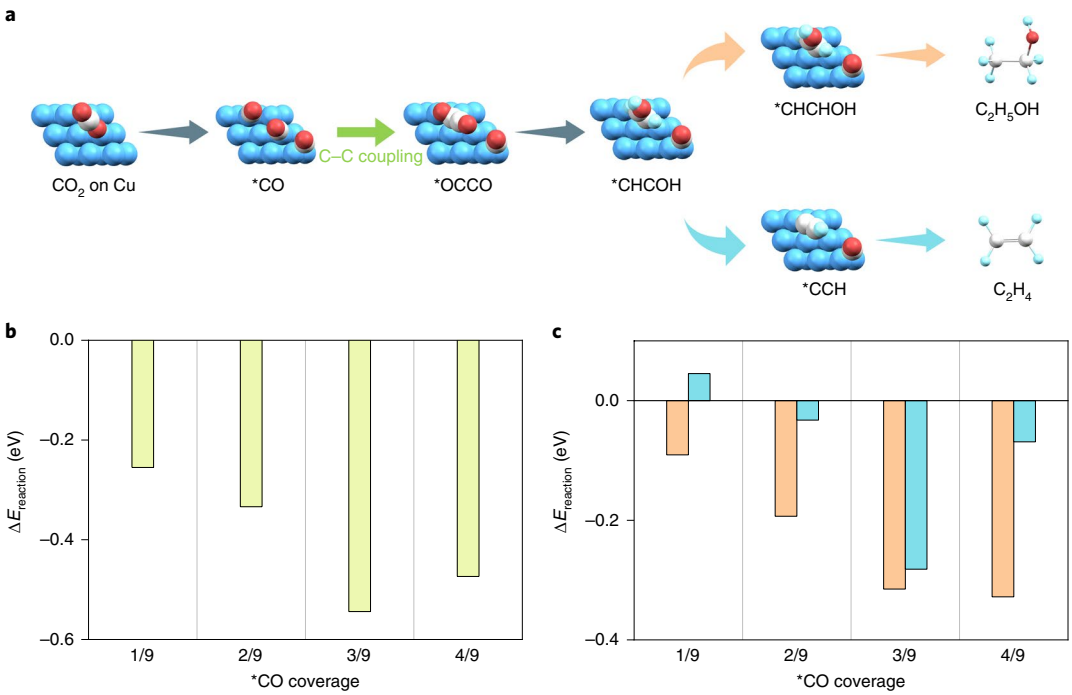

Fig. 1 | DFT calculations. a, Key reaction pathways for CO_2RR to ethanol and ethylene illustrated using two *CO for C–C coupling at the presence of one additional *CO. Blue, copper; grey, carbon; red, oxygen; light blue, hydrogen. **b**, Reaction energies ($\Delta E_{reaction}$) of two *CO forming a *OCCO via the C–C coupling step. The *CO coverage indicates the surface ratio of additional *CO on a 3×3 Cu(111) surface. **c**, Reaction energies of *CHCOH to *CHCHOH (orange) or *CCH (cyan) at different *CO coverage on a 3×3 Cu(111) surface.

ensuing reduction to ethanol on Cu sites. As a result of this strategy, we report CO_2-to-ethanol conversion with an FE of 41% at a partial current density of 124 mA cm^{-2}. We build a full-cell system, demonstrating the electrosynthesis of ethanol via CO_2 reduction coupled to the water oxidation reaction, with a full-cell energy efficiency (EE) of 13%.

Results

DFT calculations. We applied DFT calculations to predict the effect of local CO on the C–C coupling step. We first ascertained which type of CO (surface bound versus unbound) accounts for this effect on a Cu(111) surface (3×3 unit cell), a facet suggested by micro kinetics studies[30,31] to have low *CO coverages during electrocatalytic turnovers, offering us greater freedom to tune the coverage. We found that the presence of unbound CO did not affect the reaction energy of the coupling of two adsorbed *CO on the Cu surface (Supplementary Note 1 and Supplementary Figs. 1 and 2). Instead, the concentration of the unbound CO tuned the coverage of *CO on the Cu surface via the Langmuir isotherm model and then changed the reaction energy of the C–C coupling step (Supplementary Note 1). We then introduced various additional *CO coverage onto the Cu(111) surface with two *CO already adsorbed and compared the reaction energy of the C–C coupling step (Fig. 1a and Supplementary Fig. 3). The reaction energy was lowered when additional *CO was introduced, and the reduction in energy increased with further increase in *CO coverage with a coverage of 3/9 showing the largest margin (Fig. 1b): the adsorbate–adsorbate interaction became more marked with the increase in surface coverage[32].

We further calculated reaction energies associated with the hydrogenation of the intermediate *CHCOH towards either *CHCHOH or *CCH (Fig. 1a and Supplementary Fig. 4), a step found by Goddard and co-workers[25,33] critical to controlling the differential production of ethanol versus ethylene. We found that in the presence of *CO, the reaction energy decreased more for the formation of *CHCHOH (ethanol path) compared with that of *CCH (ethylene path). These reaction energies differentiated further with higher *CO coverage (Fig. 1c), indicating that high *CO coverage steers selectivity from ethylene to ethanol.

We found that the coverage of *CO also tuned the energy profiles of reaction intermediates on the Cu(100) surface, though the changes were not as marked as those on the Cu(111) surface (Supplementary Figs. 5–7). Noting that Cu(111) is typically the dominant facet of polycrystalline Cu substrates (an approach commonly employed in the study of Cu-based catalysts) we based our calculations on Cu(111).

CO_2RR performance. We pursued the intermediate-enrichment strategy experimentally by introducing a molecular catalyst on the surface of Cu (Fig. 2a), one that we posited would increase local CO concentration via its own electrocatalytic turnovers. Molecular catalysts have achieved near-unity FE for CO, commonly in non-aqueous solutions[34,35]. Their immobilization on conductive carbon substrates or covalent organic frameworks has enabled the translation of water-insoluble molecular catalysts to operate instead in aqueous solutions and has enabled marked increases in the turnover frequency for CO production[36–38]. The use of molecular complexes is expected to create CO-rich interfaces via conformal contact with Cu surfaces, without affecting the CO_2-to-C_{2+}-active electronics of Cu.

We used 5,10,15,20-tetraphenyl-21H,23H-porphine iron(III) chloride (FeTPP[Cl], Fig. 2b), which exhibits a high FE for CO at low overpotentials in both homogeneous and immobilized forms[35,39], as the molecular complex. We first examined CO_2-to-CO conversion of FeTPP[Cl] immobilized on carbon substrates via the π–π interaction[37], studying it in a flow cell (Supplementary Fig. 8) with a gas diffusion electrode (GDE) and employing 1 M aqueous $KHCO_3$ as the electrolyte (used throughout this study). The immobilized FeTPP[Cl] showed a clear increase of the reductive current under CO_2 atmosphere compared with N_2 atmosphere (linear

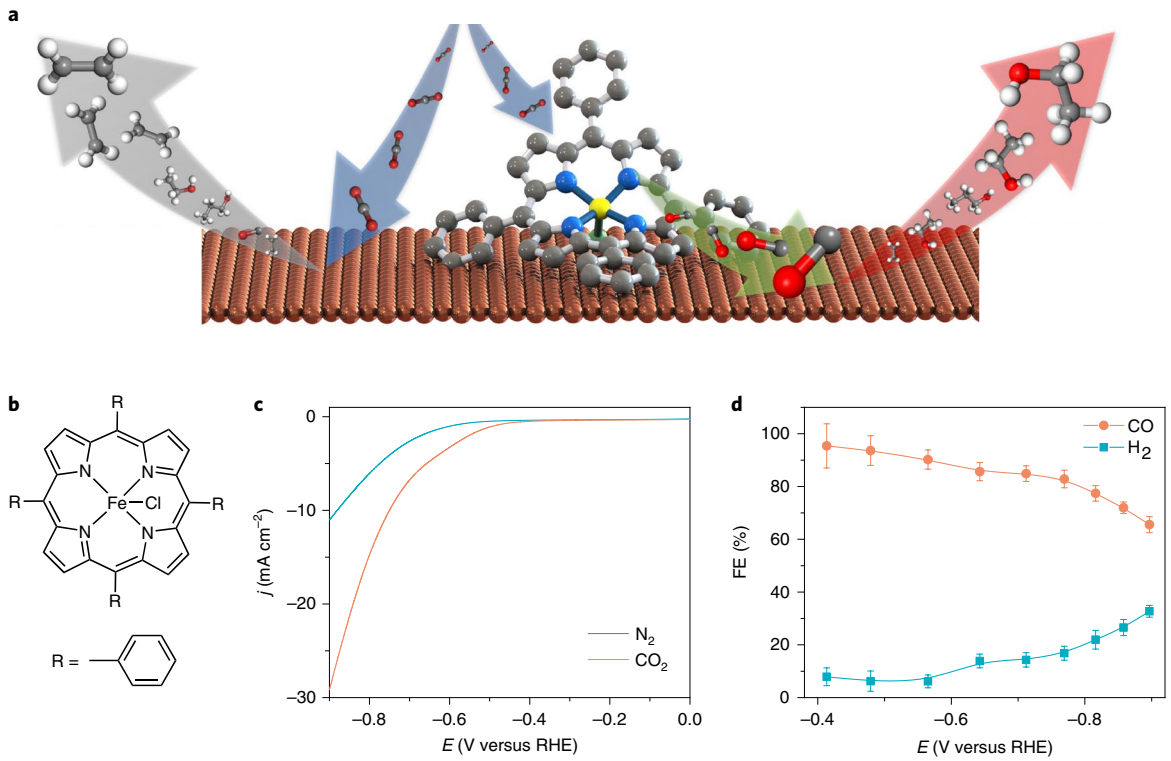

Fig. 2 | Cooperative strategy for CO_2-to-ethanol conversion. a, Schematic illustration of the heterogenization of molecular complexes on the Cu surface. The locally generated high-concentration CO favours the ethanol pathway over the ethylene pathway on the bare Cu surface. **b**, Molecular structure of the FeTPP[Cl] complex. **c**, Linear sweep voltammetry curves of FeTPP[Cl] immobilized on GDE under N_2 or CO_2 atmosphere, where *j* is total current density normalized by geometric area, and *E* is applied potential. **d**, FE of CO and H_2 of the FeTPP[Cl] catalyst immobilized on GDE under CO_2 atmosphere. The experiments were carried out in a GDE-based flow cell using 1 M $KHCO_3$ as an electrolyte. The error bars represent 1 s.d. on the basis of three independent samples.

sweep voltammetry curves, Fig. 2c), indicating a catalytic response towards CO_2RR. To evaluate quantitively the CO_2RR ability of the FeTPP[Cl], we analysed the products using gas chromatography. We found that the FE of CO was above 60% over a wide potential range with an onset potential (defined as the most positive potential at which CO product is identified by gas chromatography) of −0.41 V versus the reversible hydrogen electrode (RHE; all potentials were with respect to this reference; Fig. 2d), which matched the applied potentials typical for CO_2RR on Cu, thus promising sufficient CO supply for the ensuing C–C coupling step.

We then immobilized the FeTPP[Cl] on a Cu electrode sputtered on a hydrophobic porous polytetrafluoroethylene (PTFE) substrate (Supplementary Fig. 9)[10]. The surface-functionalized FeTPP[Cl]/Cu assembly was sufficiently stable to carry out electrochemical studies over extended operating times under reductive applied potentials, a feature we attribute to the insoluble and hydrophobic nature[40] of the FeTPP[Cl] molecule. The hydrophobic nature of the FeTPP[Cl] permitted the use of air brushing to tune its loading amount on Cu. The calculated binding of CO to the FeTPP[Cl] was weaker compared with that to the Cu(111) substrate by a margin of 0.2 eV (Supplementary Fig. 10), suggesting that the locally produced CO on the FeTPP[Cl] sites was readily spilled over onto the CO_2-to-C_{2+} active Cu sites. The modification of the FeTPP[Cl] molecular layer did not block reactants from reaching the Cu surface, which we confirmed using Raman spectroscopy and using water as the probe molecule (Supplementary Fig. 11). The morphology of Cu did not change, nor did we find the aggregation of FeTPP[Cl] to particles, when we investigated the materials using scanning electron microscopy, transmission electron microscopy and energy-dispersive X-ray elemental mapping (Supplementary Fig. 12).

We evaluated the CO_2RR performance of the FeTPP[Cl]/Cu catalyst in the electrochemical flow cell system[10]. The catalyst showed an onset potential for ethanol at −0.42 V, at which potential we started to identify ethanol with the aid of ^{1}H nuclear magnetic resonance (NMR) spectroscopy (Supplementary Fig. 13). In comparison, ethanol was detected in the case of the bare Cu electrode only when the applied potentials were more negative than −0.50 V (Fig. 3a). The selectivity of C_{2+} products, including ethanol, increased when the applied potentials became more negative, a finding we attributed to the increased electrochemical driving force[30,41]. The ethanol FE for the FeTPP[Cl]/Cu catalyst was higher than that for the bare Cu electrode across the entire applied potential range and achieved a peak value of 41% at −0.82 V (Fig. 3a). In contrast, the peak ethanol FE for the bare Cu reached only 29% at a more negative potential of −0.84 V. We confirmed, using labelled $^{13}CO_2$, that the carbon source of ethanol was CO_2 (Supplementary Fig. 14). The lower onset potential and higher FE resulted in higher ethanol current densities for the FeTPP[Cl]/Cu catalyst compared with those for pure Cu; indeed, greater than 100 mA cm^{-2} was achieved (Fig. 3b). We ascribed this increase in reaction rate to the enhanced CO_2-to-ethanol kinetics, in addition to much more abundant CO_2/electrolyte/catalyst three-phase interfaces in the GDEs compared with traditional H cells[42].

The low overpotentials and high ethanol FE resulted in high efficiency for ethanol production. The maximum half-cell CEE (see Methods for calculation details) for the FeTPP[Cl]/Cu catalyst was 23% (Fig. 3c), 1.4-fold higher than that for pure Cu under similar conditions (16%) and 1.5-fold higher than the value previously published for the case of neutral electrolyte[20]. The FeTPP[Cl]/Cu catalyst outperformed the reported catalysts in onset potential,

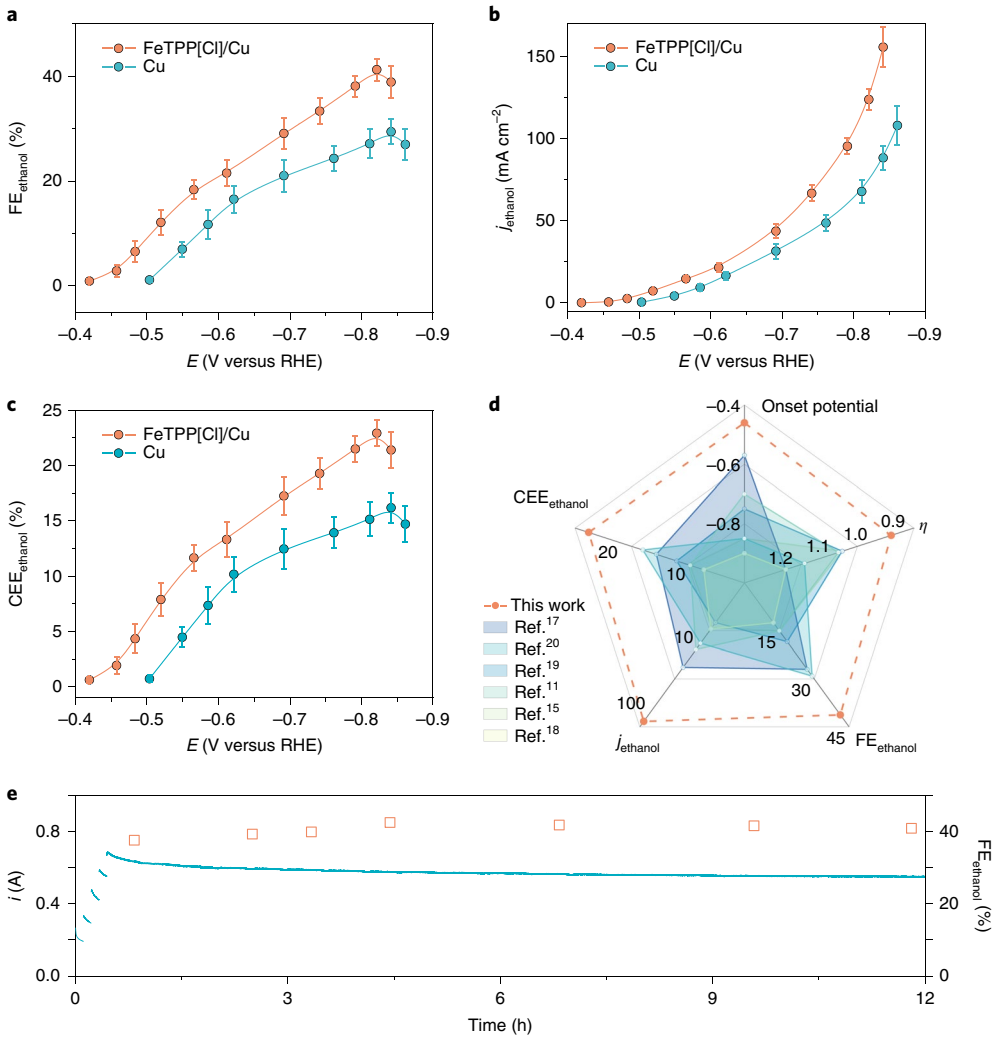

Fig. 3 | CO_2-to-ethanol conversion performance. a–c, Ethanol FE (**a**), partial current density (**b**) and half-cell CEE (**c**) over applied potentials of the FeTPP[Cl]/Cu and Cu catalysts. $j_{ethanol}$ is the ethanol partial current density normalized by geometric area. The error bars represent 1 s.d. on the basis of three independent samples. The experiments were carried out in a GDE-based flow cell using 1 M $KHCO_3$ as the electrolyte. **d**, Comparison of the onset potential, overpotential (η), FE, ethanol partial current density and half-cell CEE of the FeTPP[Cl]/Cu catalyst with those of state-of-the-art Cu-based catalysts. Only reports with a total current density >10 mA cm^{-2} were compared. **e**, Extended electrosynthesis of ethanol using the FeTPP[Cl]/Cu catalyst in a MEA system using 0.1 M $KHCO_3$ as the anolyte. *i*, total current. The full-cell voltage was gradually increased from 3 V to 3.7 V and kept constant over the course of electrolysis.

overpotential, FE, partial current density and half-cell CEE (Fig. 3d and Supplementary Table 1). The CO_2-to-ethanol activity normalized to the electrochemical surface area was also one order of magnitude higher than that in previous reports (Supplementary Table 1), in part benefitting from the flow cell we used herein. The use of neutral electrolyte circumvented the carbonate formation issue encountered in CO_2RR electrolysers using alkaline electrolytes[42].

We further integrated the CO_2 reduction and H_2O oxidation reactions in a system employing a membrane electrode assembly (MEA; Supplementary Fig. 15) to carry out the full electrosynthesis of ethanol from CO_2 and water via the reaction:

$$2CO_2 + 3H_2O \rightarrow C_2H_5OH + 3O_2 \quad E^o = 1.14 \qquad (1)$$

We operated the system for an initial 12 h at a full-cell voltage of 3.7 V. The system delivered a stable current of 0.6 A and an average ethanol FE of 41% (Fig. 3e). Thus, we obtained a full-cell EE (see Methods for calculation details) of 13%. This value is reported without the benefit of ohmic resistance (*iR*) corrections.

We observed a decrease of ethanol selectivity after the initial 12 h (Supplementary Fig. 16), which we attributed to the mass loss of the FeTPP[Cl] molecules on the Cu substrate (Supplementary Note 2 and Supplementary Figs. 17 and 18). Nevertheless, we observed no structural damage of the FeTPP[Cl] molecules (such as decomposition to nanoparticles) following electrolysis when we studied the catalyst using ultraviolet-visible absorption and X-ray absorption spectroscopies (Supplementary Fig. 18).

Mechanistic investigations. To investigate the origins of the improved ethanol selectivity of FeTPP[Cl]/Cu, we reported the combined FE of major C_2 products (ethanol and ethylene) against applied potential (Fig. 4a). We found that the combined C_2 FE for the FeTPP[Cl]/Cu catalyst was higher than that for the pure Cu electrode. Further analysis of the product distribution (Supplementary Fig. 19) indicated that the C_2 selectivity increased mainly at the expense of CO. We further compared the ratio of ethanol FE to ethylene FE. We found that, across the entire applied potential range, the FeTPP[Cl]/Cu electrode favoured ethanol over ethylene

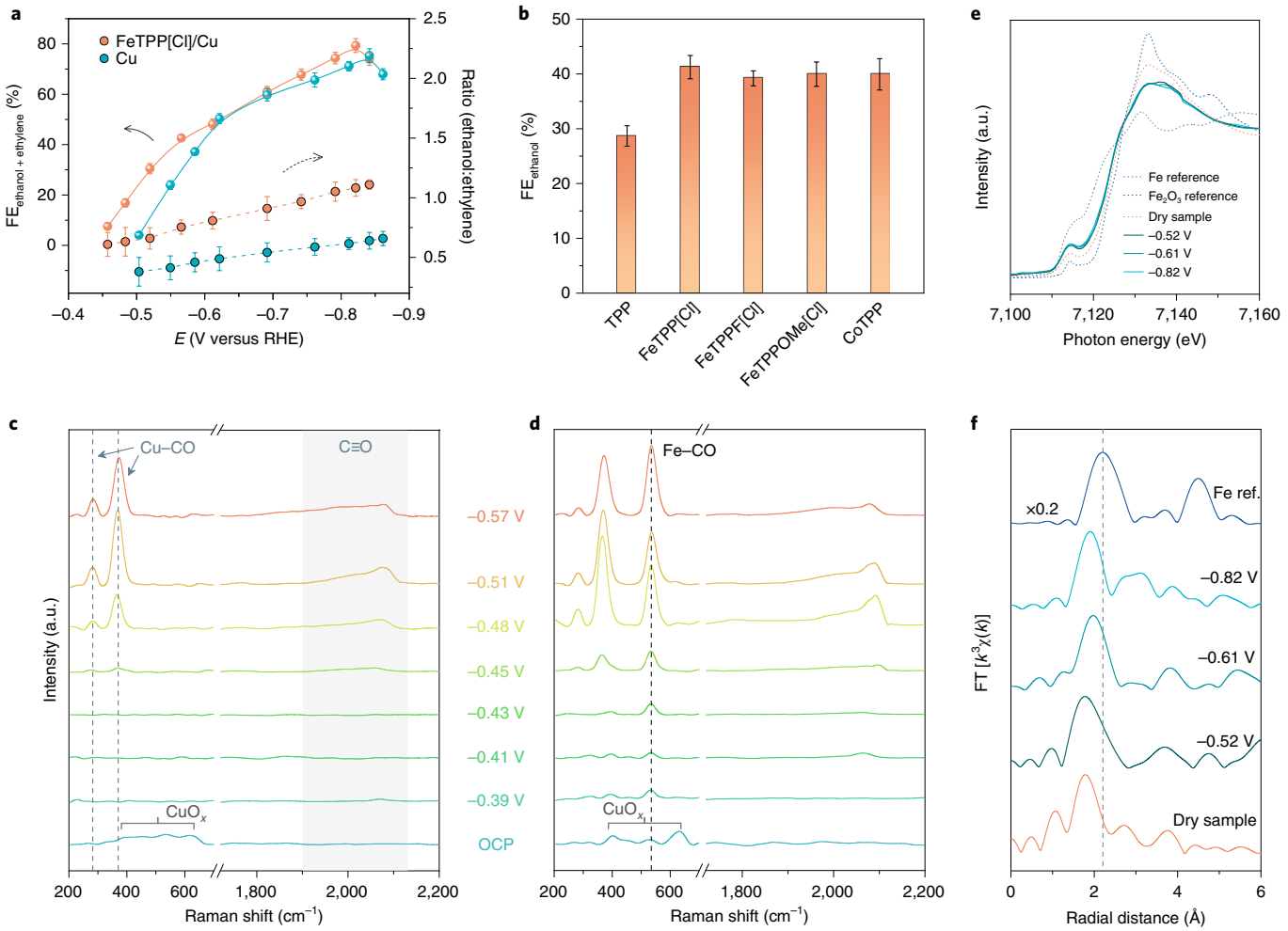

Fig. 4 | Mechanistic investigations of the FeTPP[Cl]/Cu catalyst for CO_2-to-ethanol conversion. a, FE of major C_2 products (ethanol and ethylene) and ratio of ethanol to ethylene for the FeTPP[Cl]/Cu and Cu catalysts at different applied potentials. The error bars represent 1 s.d. on the basis of three independent samples. **b**, Ethanol FE of the Cu electrode modified by different molecules. FeTPPF[Cl], 5,10,15,20-tetrakis(pentafluorophenyl)-21H,23H-porphyrin iron(III) chloride; FeTPPOMe[Cl], 5,10,15,20-tetrakis(4-methoxyphenyl)-21H,23H-porphine iron(III) chloride; CoTPP, 5,10,15,20-tetraphenyl-21H,23H-porphine cobalt(II). The error bars represent 1 s.d. on the basis of three independent samples. **c**,**d**, In situ Raman spectra of the Cu (**c**) and FeTPP[Cl]/Cu (**d**) catalysts under different applied potentials. OCP, open-circuit potential. a.u., arbitrary units. **e**,**f**, Operando Fe K-edge XANES (**e**) and EXAFS (**f**) spectra of the FeTPP[Cl]/Cu catalyst under different applied potentials.

(Fig. 4a); the ratio of ethanol to ethylene increased from approximately 0.5 for pure Cu to approximately 1 for the FeTPP[Cl]/Cu. The ratio was also larger than the values previously reported for Cu catalysts (Supplementary Table 1). These results were consistent with DFT calculations, in which high CO coverage favoured the ethanol pathway over the ethylene pathway.

To explore whether the local high-concentration CO directly contributed to the enhanced ethanol selectivity, we modified the Cu electrode with the molecule Ni-tetraphenylporphyrin (TPP; NiTPP), whose CO_2-to-CO conversion onset potential was more negative than that of the FeTPP[Cl] molecule (Supplementary Fig. 20). We found that only after the NiTPP started to generate CO did the ethanol FE show marked improvement on the NiTPP/Cu catalyst (Supplementary Fig. 20). This agrees with the view that improved ethanol selectivity arises from local CO enrichment.

We further investigated the role of the FeTPP[Cl] molecule by varying its loading on the Cu substrate. We found that both the combined C_2 FE and the ratio of ethanol to ethylene gradually increased against the surface coverage (see quantification details in Supplementary Note 3 and Supplementary Fig. 21) of the FeTPP[Cl] on the Cu and reached the maximum values when the coverage was near 1. This trend suggested that the locally concentrated CO provided by the FeTPP[Cl] enhanced the ethanol selectivity in CO_2RR. A further increase of the FeTPP[Cl] coverage led to decreased ethanol selectivity, which we accounted for by noting that too few Cu sites were available for C–C coupling, in agreement with the observed increased CO FE. We highlighted that the additional layer of molecular catalyst on Cu allowed the ratio of *CO-producing sites to C–C coupling sites to approach unity. In contrast, the heteroatom doping strategy was limited to an analogous ratio of approximate 0.02 in the Au/Cu bimetallic catalyst[27]. We noted also that the *CO-enrichment strategy was expected to substantially leave the electronic properties of Cu unchanged, in contrast with the elemental alloying approach[29].

We carried out control studies to examine whether ethanol selectivity was influenced by the porphyrin framework itself. Using in situ Raman spectroscopy, we found that the TPP framework did not tune the binding properties of the Cu substrate to CO (Supplementary Fig. 22). We found no enhancement of ethanol selectivity for the TPP/Cu electrode (Fig. 4b). These observations

agreed with the main role for the FeTPP[Cl] complex as a CO_2-to-CO conversion enhancer. This view was further supported by the fact that a family of CO_2-to-CO catalytically active porphyrin-based complexes with different ligand structures and cobalt centres also showed enhanced performance for CO_2-to-ethanol (Fig. 4b and Supplementary Fig. 23). The range of molecular enhancers demonstrated here showcases the wider applicability of the homogeneous–heterogeneous cooperative strategy in reprogramming CO_2RR.

Taking these experimental findings together with the DFT calculations, we conclude that the functional complexes in this study generate a CO-rich environment at the molecule–metal interface, increasing the coverage of *CO on the Cu surface. This lowers the barrier to C–C coupling and steers selectivity towards ethanol, resulting in increased control over CO_2RR.

To gain molecular-level insight into the cooperative role of the heterogenized FeTPP[Cl] and Cu substrate, we interrogated the FeTPP[Cl]/Cu surface using in situ Raman spectroscopy (Supplementary Fig. 24). We acquired Raman spectra on both Cu and FeTPP[Cl]/Cu electrodes at a range of applied potentials from the open-circuit potential to −0.57 V (Fig. 4c, d). Under negative applied potentials, the peaks associated with surface copper oxide (CuO_x) disappeared, a finding we attributed to the reduction of the oxide to metallic Cu.

On bare Cu electrodes, three bands were identified associated with surface-adsorbed *CO at 280, 365 and the range of 1,900–2,130 cm^{-1} (Fig. 4c). These bands emerged at −0.45 V and corresponded to the Cu–CO frustrated rotation, the Cu–CO stretch and the C≡O stretch, respectively[43,44]. On the FeTPP[Cl]/Cu catalyst, the same bands emerged at an earlier onset potential of −0.41 V (Fig. 4d); this was consistent with the notion that CO concentration was enhanced on the FeTPP[Cl]/Cu electrode. We also observed an emerging band at 535 cm^{-1}, which we attributed to the Fe–CO bending vibration owing to the interaction between CO and Fe in the iron porphyrin segment[45–47]. This finding supports the view that immobilized FeTPP[Cl] produced CO, which was then converted to C_{2+} products on a nearby Cu site, as evidenced by the Cu–CO feature and by the fact that the FE of CO on FeTPP[Cl]/Cu did not increase compared with that on bare Cu at similar applied potentials. This view agreed with the picture of cooperative electrocatalytic CO_2-to-ethanol conversion by the heterogenized FeTPP[Cl] on the Cu substrate in Fig. 2a. We confirmed, carrying out Ar and $^{13}CO_2$ controls (Supplementary Fig. 25), that the Raman peaks corresponding to Cu–CO and Fe–CO as discussed above were indeed from CO_2RR. The band at 535 cm^{-1} was ruled out as being from CuO_x using X-ray absorption spectroscopy (XAS; vide infra).

We investigated further the chemical structure and coordinating environment of FeTPP[Cl] under operating conditions using XAS. The Fe K-edge X-ray absorption near edge structure (XANES) spectra of the FeTPP[Cl]/Cu showed that the central Fe ions of the FeTPP[Cl] molecules were slightly reduced under catalytic turnover conditions (Fig. 4e). Using linear combination fitting, we calculated the average oxidation state of Fe to be ~1.7–1.8 under operating conditions (Supplementary Fig. 26), consistent with the reported mechanism for the electrochemical CO_2-to-CO conversion by FeTPP[Cl], where the porphyrin-coordinated Fe^{2+}, Fe^{1+} and Fe^0 were supposed to be intermediate species[48,49]. We also observed a higher pre-edge feature compared with that for the dry sample, a finding suggesting a more distorted structure by coordination of the metal centre with CO_2RR intermediates[50]. We examined the Fe K-edge extended X-ray absorption fine structure (EXAFS) spectra of the FeTPP[Cl]/Cu catalyst. Over the applied potential range relevant to CO_2RR, we identified only the Fe–N bond, whereas the Fe–Fe bond was not observed (Fig. 4f). This finding suggests that FeTPP[Cl] maintained its original complex status instead of being reduced to iron nanoparticles or nanoclusters under operating conditions. The stability of the FeTPP[Cl] molecule was further supported by its reversibility following electrolysis; the oxidation state of Fe recovered to the same value as that before the reaction and there was no Fe–Fe bond formation, findings we obtained examining the post-electrolysis catalyst using XAS (Supplementary Fig. 18). With the aid of both Cu K-edge XANES and EXAFS spectroscopies, we confirmed that Cu remained in the metallic state and that the porphyrin did not coordinate with Cu under catalytically active conditions (Supplementary Fig. 27).

Conclusions

In summary, we present an intermediate-enrichment-enhanced electrocatalytic CO_2-to-ethanol conversion strategy by cooperative catalysis at the molecule–metallic interface. Using this strategy, implemented using a family of porphyrin-based metallic complexes on a Cu catalyst, we reported a CO_2-to-ethanol conversion with an ethanol FE of 41% at a partial current density of 124 mA cm^{-2} in neutral media. We achieved a full-cell EE of 13% for the electrosynthesis of ethanol from CO_2 and water. The findings suggest a wider strategy for improving CO_2 conversion into value-added liquid fuels using renewable electricity with the aid of cooperative effects between adsorbed molecular and heterogeneous approaches.

Methods

DFT calculations. All the DFT calculations in this work were carried out with a periodic slab model using the Vienna ab initio simulation program[51–54]. The generalized gradient approximation was used with the Perdew–Burke–Ernzerhof[55] exchange-correlation functional. The projector-augmented wave method[56,57] was utilized to describe the electron–ion interactions and the cut-off energy for the plane–wave basis set was 450 eV. To illustrate the long-range dispersion interactions between the adsorbates and catalysts, we employed the D3 correction method as described by Grimme et al.[58]. Brillouin zone integration was accomplished using a 3×3×1 Monkhorst–Pack *k*-point mesh. All the adsorption geometries were optimized using a force-based conjugate gradient algorithm. For the modelling of Cu(111) and Cu(100), the crystal structure was optimized; Cu(111) and Cu(100) were modelled with a periodic four-layer p(3×3) model with the two lower layers fixed and the two upper layers relaxed. FeTPP[Cl]/Cu(111) was modelled with a periodic three-layer p(9×9) model with the one lower layer fixed and two upper layers relaxed. The atomic coordinates of the optimized models are provided in Supplementary Data 1.

Electrode preparation. All chemicals were purchased from Sigma Aldrich and were used without further purification. The PTFE electrode was prepared by sputtering 200 nm Cu onto a piece of PTFE membrane (pore size of 450 nm, with a polypropylene support on the backside) using a pure Cu target (99.99%) at a sputtering rate of 0.67 Å s^{-1}. The porphyrin-based complexes were dissolved in a mixture of tetrahydrofuran and acetonitrile (6:4 by volume) at a concentration of 0.1 mM. The complexes were then spray-coated on either GDE (Sigracet, Fuel Cell Store) or the PTFE electrode. The nominal concentration was estimated on the basis of the concentration of solution used for the spray coat and the true loading concentration was quantified by inductively coupled plasma mass spectrometry (ICP–MS; Supplementary Fig. 21). The optimized loading of the FeTPP[Cl] molecules for the GDE was approximately fivefold higher than that for the Cu/PTFE electrode owing to the larger surface area of the GDE.

CO_2RR and product analysis. Most CO_2RR measurements were conducted in an electrochemical flow cell setup (details in Supplementary Fig. 8). The applied potentials were converted to the RHE scale with *iR* correction through the following equation:

$$E_{RHE} = E_{versus\ Ag/AgCl} + 0.059 \times pH + 0.210 + iR \quad (2)$$

where *i* is the current at each applied potential and *R* is the equivalent series resistance measured via electrochemical impedance spectroscopy in the frequency range of 10^5–0.1 Hz with an amplitude of 10 mV.

The MEA (see details in Supplementary Fig. 15) system was used to carry out the full electrosynthesis of ethanol. The full-cell voltage was gradually increased from 3 V to 3.7 V and kept constant over the course of electrolysis.

The gaseous products were analysed by gas chromatography (PerkinElmer Clarus 600), equipped with a thermal conductivity detector and a flame ionization detector. Liquid products were quantified by ^1H NMR spectroscopy (600 MHz Agilent DD2 NMR spectrometer) using dimethyl sulfoxide as the internal standard. Isotopic experiments were carried out using 1 M KCl and 1 M $KHCO_3$ as catholyte and anolyte, respectively, to avoid the exchange of carbon between $^{13}CO_2$ and $H^{12}CO_3^-$.

EE was calculated on the basis of the cathodic CO_2RR coupled with anodic water oxidation reaction (O_2+4H$^+$ + 4e$^-$ ↔ 2H_2O; 1.23 V versus RHE).

$$EE = \frac{E_{ox^o} - E_{red^o}}{E_{ox} - E_{red}} \times FE_{ethanol} \quad (3)$$

where E_{ox^o} and E_{red^o} are the thermodynamic potentials for water oxidation and CO_2RR to ethanol (0.09 V versus RHE), respectively and E_{ox} and E_{red} are the applied potentials at anode and cathode, respectively. For the calculation of the half-cell CEE, the anodic reaction was assumed to occur with an overpotential of 0 V (that is E_{ox} = 1.23 V). For full-cell EE calculation, the equation then was simplified to

$$EE_{full\ cell} = \frac{E^o}{E_{full\ cell}} \times FE_{ethanol} \quad (4)$$

where $E_{full\ cell}$ is the applied voltage of the MEA system and $E^o = E_{ox^o} - E_{red^o}$.

Materials characterization. Scanning electron microscopy was performed using a Hitachi S-5200. X-ray photoelectron spectroscopy measurements were carried out using a Thermo Scientific K-Alpha spectrophotometer with a monochromated Al Kα X-ray radiation source. X-ray diffraction patterns were recorded on a Rigaku MiniFlex600 G6. ICP–MS was measured on a Bruker Aurora M90. Hard XAS measurements were performed using a modified flow cell[59] at the 9BM beamline of the Advanced Photon Source located in the Argonne National Laboratory. XAS data were processed with Demeter (v.0.9.26)[60]. In situ Raman measurements were carried out using a Renishaw inVia Raman microscope in a modified flow cell (Supplementary Fig. 24) with a water immersion objective. A 785-nm laser was used and signals were recorded using a 5-s integration and by averaging five scans. The gas (CO_2, Ar and $^{13}CO_2$) with a flow rate of 40 standard cm^3 min^{-1} was flowed through the cell for corresponding experiments. An Ag/AgCl (3 M KCl) electrode and a Pt wire were used as the reference and counter electrodes, respectively, in all measurements.

Data availability

The datasets generated during, and/or analysed during, the present study, are available from the corresponding author on reasonable request.

Received: 26 April 2019; Accepted: 14 October 2019;
Published online: 16 December 2019

References

1. Ross, M. B. et al. Designing materials for electrochemical carbon dioxide recycling. *Nat. Catal.* **2**, 648–658 (2019).
2. Birdja, Y. Y. et al. Advances and challenges in understanding the electrocatalytic conversion of carbon dioxide to fuels. *Nat. Energy* **4**, 732–745 (2019).
3. Shih, C. F., Zhang, T., Li, J. & Bai, C. Powering the future with liquid sunshine. *Joule* **2**, 1925–1949 (2018).
4. Spurgeon, J. & Kumar, B. A comparative technoeconomic analysis of pathways for commercial electrochemical CO_2 reduction to liquid products. *Energy Environ. Sci.* **11**, 1536–1551 (2018).
5. Hori, Y. in *Modern Aspects of Electrochemistry* Vol. 42 (eds Vayenas, C. G. et al.) 89–189 (Springer, 2008).
6. Gao, D., Arán-Ais, R. M., Jeon, H. S. & Roldan Cuenya, B. Rational catalyst and electrolyte design for CO_2 electroreduction towards multicarbon products. *Nat. Catal.* **2**, 198–210 (2019).
7. Kortlever, R., Shen, J., Schouten, K. J., Calle-Vallejo, F. & Koper, M. T. Catalysts and reaction pathways for the electrochemical reduction of carbon dioxide. *J. Phys. Chem. Lett.* **6**, 4073–4082 (2015).
8. Kuhl, K. P., Cave, E. R., Abram, D. N. & Jaramillo, T. F. New insights into the electrochemical reduction of carbon dioxide on metallic copper surfaces. *Energy Environ. Sci.* **5**, 7050–7059 (2012).
9. Ma, S. et al. One-step electrosynthesis of ethylene and ethanol from CO_2 in an alkaline electrolyzer. *J. Power Sources* **301**, 219–228 (2016).
10. Dinh, C.-T. et al. CO_2 electroreduction to ethylene via hydroxide-mediated copper catalysis at an abrupt interface. *Science* **360**, 783–787 (2018).
11. Jiang, K. et al. Metal ion cycling of Cu foil for selective C–C coupling in electrochemical CO_2 reduction. *Nat. Catal.* **1**, 111–119 (2018).
12. Clark, E. L., Hahn, C., Jaramillo, T. F. & Bell, A. T. Electrochemical CO_2 reduction over compressively strained CuAg surface alloys with enhanced multi-carbon oxygenate selectivity. *J. Am. Chem. Soc.* **139**, 15848–15857 (2017).
13. Hoang, T. T. H. et al. Nano porous copper-silver alloys by additive-controlled electro-deposition for the selective electroreduction of CO_2 to ethylene and ethanol. *J. Am. Chem. Soc.* **140**, 5791–5797 (2018).
14. Li, C. W., Ciston, J. & Kanan, M. W. Electroreduction of carbon monoxide to liquid fuel on oxide-derived nanocrystalline copper. *Nature* **508**, 504–507 (2014).
15. Zhuang, T.-T. et al. Steering post-C–C coupling selectivity enables high efficiency electroreduction of carbon dioxide to multi-carbon alcohols. *Nat. Catal.* **1**, 421–428 (2018).
16. Jouny, M., Luc, W. W. & Jiao, F. General techno-economic analysis of CO_2 electrolysis systems. *Ind. Eng. Chem. Res.* **57**, 2165–2177 (2018).
17. Zhou, Y. et al. Dopant-induced electron localization drives CO_2 reduction to C_2 hydrocarbons. *Nat. Chem.* **10**, 974–980 (2018).
18. De Luna, P. et al. Catalyst electro-redeposition controls morphology and oxidation state for selective carbon dioxide reduction. *Nat. Catal.* **1**, 103–110 (2018).
19. Liang, Z.-Q. et al. Copper-on-nitride enhances the stable electrosynthesis of multi-carbon products from CO_2. *Nat. Commun.* **9**, 3828 (2018).
20. Ren, D., Ang, B. S.-H. & Yeo, B. S. Tuning the selectivity of carbon dioxide electroreduction toward ethanol on oxide-derived Cu_xZn catalysts. *ACS Catal.* **6**, 8239–8247 (2016).
21. Vojvodic, A. & Nørskov, J. K. New design paradigm for heterogeneous catalysts. *Natl Sci. Rev.* **2**, 140–143 (2015).
22. Peterson, A. A. & Nørskov, J. K. Activity descriptors for CO_2 electroreduction to methane on transition-metal catalysts. *J. Phys. Chem. Lett.* **3**, 251–258 (2012).
23. Calle-Vallejo, F. & Koper, M. T. Theoretical considerations on the electroreduction of CO to C_2 species on Cu(100) electrodes. *Angew. Chem. Int. Ed.* **52**, 7282–7285 (2013).
24. Montoya, J. H., Shi, C., Chan, K. & Nørskov, J. K. Theoretical insights into a CO dimerization mechanism in CO_2 electroreduction. *J. Phys. Chem. Lett.* **6**, 2032–2037 (2015).
25. Xiao, H., Cheng, T. & Goddard, W. A. Atomistic mechanisms underlying selectivities in C_1 and C_2 products from electrochemical reduction of CO on Cu(111). *J. Am. Chem. Soc.* **139**, 130–136 (2017).
26. Lee, S., Park, G. & Lee, J. Importance of Ag–Cu biphasic boundaries for selective electrochemical reduction of CO_2 to ethanol. *ACS Catal.* **7**, 8594–8604 (2017).
27. Morales-Guio, C. G. et al. Improved CO_2 reduction activity towards C_{2+} alcohols on a tandem gold on copper electrocatalyst. *Nat. Catal.* **1**, 764–771 (2018).
28. Ma, S. et al. Electroreduction of carbon dioxide to hydrocarbons using bimetallic Cu–Pd catalysts with different mixing patterns. *J. Am. Chem. Soc.* **139**, 47–50 (2017).
29. Kim, D., Resasco, J., Yu, Y., Asiri, A. M. & Yang, P. Synergistic geometric and electronic effects for electrochemical reduction of carbon dioxide using gold-copper bimetallic nanoparticles. *Nat. Commun.* **5**, 4948 (2014).
30. Liu, X. et al. pH effects on the electrochemical reduction of $CO_{(2)}$ towards C_2 products on stepped copper. *Nat. Commun.* **10**, 32 (2019).
31. Liu, X. et al. Understanding trends in electrochemical carbon dioxide reduction rates. *Nat. Commun.* **8**, 15438 (2017).
32. Lausche, A. C. et al. On the effect of coverage-dependent adsorbate–adsorbate interactions for CO methanation on transition metal surfaces. *J. Catal.* **307**, 275–282 (2013).
33. Cheng, T., Xiao, H. & Goddard, W. A. Full atomistic reaction mechanism with kinetics for CO reduction on Cu(100) from ab initio molecular dynamics free-energy calculations at 298 K. *Proc. Natl Acad. Sci. USA* **114**, 1795–1800 (2017).
34. Costentin, C., Drouet, S., Robert, M. & Savéant, J. M. A local proton source enhances CO_2 electroreduction to CO by a molecular Fe catalyst. *Science* **338**, 90–94 (2012).
35. Costentin, C., Robert, M. & Savéant, J. M. Catalysis of the electrochemical reduction of carbon dioxide. *Chem. Soc. Rev.* **42**, 2423–2436 (2013).
36. Lin, S. et al. Covalent organic frameworks comprising cobalt porphyrins for catalytic CO_2 reduction in water. *Science* **349**, 1208–1213 (2015).
37. Hu, X. M., Rønne, M. H., Pedersen, S. U., Skrydstrup, T. & Daasbjerg, K. Enhanced catalytic activity of cobalt porphyrin in CO_2 electroreduction upon immobilization on carbon materials. *Angew. Chem. Int. Ed.* **56**, 6468–6472 (2017).
38. Zhang, X. et al. Highly selective and active CO_2 reduction electrocatalysts based on cobalt phthalocyanine/carbon nanotube hybrid structures. *Nat. Commun.* **8**, 14675 (2017).
39. Smith, P. T. et al. Iron porphyrins embedded into a supramolecular porous organic cage for electrochemical CO_2 reduction in water. *Angew. Chem. Int. Ed.* **57**, 9684–9688 (2018).
40. Joya, K. S., Morlanés, N., Maloney, E., Rodionov, V. & Takanabe, K. Immobilization of a molecular cobalt electrocatalyst by hydrophobic interaction with a hematite photoanode for highly stable oxygen evolution. *Chem. Commun.* **51**, 13481–13484 (2015).
41. Bertheussen, E. et al. Acetaldehyde as an intermediate in the electroreduction of carbon monoxide to ethanol on oxide-derived copper. *Angew. Chem. Int. Ed.* **55**, 1450–1454 (2016).
42. Weekes, D. M., Salvatore, D. A., Reyes, A., Huang, A. & Berlinguette, C. P. Electrolytic CO_2 reduction in a flow cell. *Acc. Chem. Res.* **51**, 910–918 (2018).
43. Sheppard, N. & Nguyen, T. T. *Advances in Infrared and Raman Spectroscopy*. (Heyden, 1978).
44. Gunathunge, C. M. et al. Spectroscopic observation of reversible surface reconstruction of copper electrodes under CO_2 reduction. *J. Phys. Chem. C.* **121**, 12337–12344 (2017).
45. Tsubaki, M., Srivastava, R. B. & Yu, N. T. Resonance Raman investigation of carbon monoxide bonding in (carbon monoxy)hemoglobin and -myoglobin:

detection of iron–carbon monoxide stretching and iron–carbon–oxygen bending vibrations and influence of the quaternary structure change. *Biochem.* **21**, 1132–1140 (1982).
46. Kerr, E. A., Mackin, H. C. & Yu, N. T. Resonance Raman studies of carbon monoxide binding to iron "picket fence" porphyrin with unhindered and hindered axial bases. An inverse relationship between binding affinity and the strength of iron–carbon bond. *Biochem.* **22**, 4373–4379 (1983).
47. Uno, T. et al. The resonance Raman frequencies of the Fe–CO stretching and bending modes in the CO complex of cytochrome P-450cam. *J. Bio. Chem.* **260**, 2023–2026 (1985).
48. Costentin, C., Drouet, S., Passard, G., Robert, M. & Savéant, J. M. Proton-coupled electron transfer cleavage of heavy-atom bonds in electrocatalytic processes. Cleavage of a C–O bond in the catalyzed electrochemical reduction of CO_2. *J. Am. Chem. Soc.* **135**, 9023–9031 (2013).
49. Costentin, C., Passard, G., Robert, M. & Savéant, J. M. Ultraefficient homogeneous catalyst for the CO_2-to-CO electrochemical conversion. *Proc. Natl Acad. Sci. USA* **111**, 14990–14994 (2014).
50. Yang, H. B. et al. Atomically dispersed Ni(I) as the active site for electrochemical CO_2 reduction. *Nat. Energy* **3**, 140–147 (2018).
51. Kresse, G. & Furthmüller, J. Efficient iterative schemes for ab initio total-energy calculations using a plane-wave basis set. *Phys. Rev. B* **54**, 11169–11186 (1996).
52. Kresse, G. & Furthmüller, J. Efficiency of ab-initio total energy calculations for metals and semiconductors using a plane-wave basis set. *Comput. Mater. Sci.* **6**, 15–50 (1996).
53. Kresse, G. & Hafner, J. Ab initio molecular dynamics for liquid metals. *Phys. Rev. B* **47**, 558–561 (1993).
54. Kresse, G. & Hafner, J. Ab initio molecular-dynamics simulation of the liquid-metal–amorphous-semiconductor transition in germanium. *Phys. Rev. B* **49**, 14251–14269 (1994).
55. Perdew, J. P., Burke, K. & Ernzerhof, M. Generalized gradient approximation made simple. *Phys. Rev. Lett.* **77**, 3865–3868 (1996).
56. Kresse, G. & Joubert, D. From ultrasoft pseudopotentials to the projector augmented-wave method. *Phys. Rev. B* **59**, 1758–1775 (1999).
57. Blöchl, P. E. Projector augmented-wave method. *Phys. Rev. B* **50**, 17953–17979 (1994).
58. Grimme, S., Antony, J., Ehrlich, S. & Krieg, H. A consistent and accurate ab initio parametrization of density functional dispersion correction (DFT-D) for the 94 elements H-Pu. *J. Chem. Phys.* **132**, 154104 (2010).
59. Li, J. et al. Copper adparticle enabled selective electrosynthesis of n-propanol. *Nat. Commun.* **9**, 4614 (2018).
60. Ravel, B. & Newville, M. ATHENA, ARTEMIS, HEPHAESTUS: data analysis for X-ray absorption spectroscopy using IFEFFIT. *J. Synchrotron Rad.* **12**, 537–541 (2005).

Acknowledgements

The authors acknowledge funding support from Suncor Energy, the Ontario Research fund and the Natural Sciences and Engineering Research Council (NSERC). DFT computations were performed on the IBM BlueGene/Q supercomputer with support from the Niagara supercomputer at the SciNet HPC Consortium and the Southern Ontario Smart Computing Innovation Platform (SOSCIP). SciNet is funded by the Canada Foundation for Innovation, the Government of Ontario's Ontario Research Fund – Research Excellence, and the University of Toronto. SOSCIP is funded by the Federal Economic Development Agency of Southern Ontario, the Province of Ontario, IBM Canada, Ontario Centres of Excellence, Mitacs and 15 Ontario academic member institutions. This research used synchrotron resources of the Advanced Photon Source, an Office of Science User Facility operated for the US Department of Energy Office of Science by Argonne National Laboratory and was supported by the US Department of Energy under contract no. DE-AC02-06CH11357 and the Canadian Light Source and its funding partners. F.L. thanks H.T.L. for ICP–MS measurement. J.L. acknowledges the Banting Postdoctoral Fellowships programme. C.G. acknowledges the NSERC Postdoctoral Fellowships programme. D.S. acknowledges the NSERC E.W.R. Steacie Memorial Fellowship.

Author contributions

E.H.S. supervised the project. F.L. conceived the idea and carried out the experiments. F.L. and E.H.S. wrote the paper. Y.C.L. and Z.W. carried out the DFT calculations. D.H.N. and Y. Lum performed the XAS measurements. D.H.N., J.L. and S-F.H. helped to analyse the XAS data. Y. Li and A.O. carried out part of electrochemical experiments. M.L. and X.W. provided help in NMR analysis. B.C., Y.H.W., J.W., Y.X., C.-T.D., Y.W. and T.-T.Z. helped to characterize the materials. Y.C.L. and C.M.G. helped in the Raman measurements. D.S. assisted in data analysis and manuscript writing. All authors discussed the results and assisted during manuscript preparation.

Competing interests

The authors declare no competing interests.

Additional information

Supplementary information is available for this paper at https://doi.org/10.1038/s41929-019-0383-7.

Correspondence and requests for materials should be addressed to E.H.S.

Reprints and permissions information is available at www.nature.com/reprints.

Publisher's note Springer Nature remains neutral with regard to jurisdictional claims in published maps and institutional affiliations.